Effects of Surface Tension and Yield Stress on Mucus Plug Rupture: a Numerical Study

Yingying Hu, Francesco Romano, James B. Grotberg

Effects of Surface Tension and Yield Stress on Mucus Plug Rupture: a Numerical Study

Yingying Hu[*1], Francesco Romanò[2,3], James B. Grotberg[2]

[1] School of Electrical Power Engineering, China University of Mining and Technology, Xuzhou, Jiangsu 221116, China

[2] Department of Biomedical Engineering, University of Michigan, 2123 Carl A. Gerstacker Building, 2200 Bonisteel Boulevard, Ann Arbor, MI 48109-2099, USA

[3] Univ. Lille, CNRS, ONERA, Arts et Metiers ParisTech, Centrale Lille, FRE 2017-LMFL-Laboratoire de Mécanique des Fluides de Lille-Kampé de Fériet, F-59000, Lille, France

[*] Corresponding author: Email address: hyy@cumt.edu.cn (Yingying Hu), Tel.: (+86)-516-83592000.

Abstract

We study the effects of surface tension and yield stress on mucus plug rupture. A three-dimensional simplified configuration is employed to simulate mucus plug rupture in a collapsed lung airway of the 10th generation. The Herschel-Bulkley model is used to take into account the non-Newtonian viscoplastic fluid properties of mucus. Results show that the maximum wall shear stress greatly changes right prior to the rupture of the mucus plug. The surface tension influences mainly the late stage of the rupture process when the plug deforms greatly and the curvature of the mucus-air interface becomes significant. High surface tension increases the wall shear stress and the time needed to rupture since it produces a resistance to the rupture, as well as strong stress and velocity gradients across the mucus-air interface. The yield stress effects are pronounced mainly at the beginning. High yield stress makes the plug take long time to yield and slows down the whole rupture process. When the effects induced by the surface tension and yield forces are comparable, dynamical quantities strongly depend on the ratio of the two forces. The pressure difference (the only driving in the study) contributes to wall shear stress much more than yield stress and surface tension per unit length. Wall shear stress is less sensitive to the variation in yield stress than that in surface tension. In general, wall shear stress can be effectively reduced by the smaller pressure difference and surface tension.

Keywords: Mucus plug rupture, Herschel-Bulkley model, yield stress, surface tension, wall shear stress.

1 Introduction

Mucus plug rupture involves mucus clearance in lung airways, especially in a diseased lung, where mucus is often hypersecreted. Typical pathological conditions involve, indeed, a thick layer of mucus characterized by high viscosity and yield stress. This penalizes the clearance process and may result in bacteria accumulation, infections, and other collateral complications. Maintaining a normal level of mucus clearance is therefore necessary for a healthy lung function. However, mucus plug rupture, necessary for the mucus clearance of occluded airways, may generate high shear stresses and potentially damage the epithelial cells which cover airway walls (Bilek 2003; Kay 2004; Bertram 2005; Huh 2007).

The research about plug formation, propagation and rupture in human and animal airways has been a fruitful field of fluid mechanics for several decades. The thickness of the mucus film lining the airways is regarded as one of the key factors in plug formation and rupture. If the film thickness is greater than a certain (critical) value, the Plateau-Rayleigh instability amplifies the perturbation of the mucus-air interface leading to the formation of a liquid plug which occludes the passage lumen of the airway (Halpern 1992; Romanò 2019). When considering wet airways, i.e. liquid-lined bronchioles, if the trailing

film is thicker than the precursor film, a plug traveling along the airway drains the liquid mass from the plug and transfers it to the film, up to airway reopening due to plug rupture; on the other hand, if the trailing is thinner than the precursor film, the mucus plug grows and the plug propagation is stable (Fujioka 2004 and 2008; Hassan 2011; Magniez 2016). When almost dry airways are considered, the plug ruptures if the initial precursor film is less than one tenth of the passage radius (Hassan 2011). The front meniscus of a moving plug is characterized by the maximum of the wall shear and pressure stress (Fujioka 2004) and the stresses reach their peaks right after rupture (Hassan 2011; Muradoglu 2019). Plugs, especially large ones, are more likely to break under cyclic forcing than unidirectional pressure forcing, in which two instability mechanisms may work, namely the decreasing of viscous resistance with plug length shortening and the reduction of the plug interfacial resistance related to lubrication effects (Mamba 2018). Wall compliance of highly collapsed channels may be favorable to the break-up of fast-propagating plugs, since the displacement of the elastic channel wall enhances the instability leading to rupture (Ducloue 2017).

Surface tension between mucus and air is an influential factor in plug rupture. Upon a reduction of the surface tension, the peaks of shear stress and pressure reduce, too. The same trend is observed for the axial component of the stress gradient, as well as the plug propagation speed and the travel distance prior to rupture (Fujioka 2008). Decreasing surface tension promotes film thickening, hence liquid plug formation, and consequently airway occlusion (Halpern 1992; Roman ò 2019). Related to surface tension, an often-concerned topic is rupture of plugs laden with surfactant, which is clinically relevant in treatment of premature neonates with surfactant deficiency (Ellyett 2006; Carnielli 2009; Willson 2011). With propagation of a surfactant-laden plug, surfactant accumulates on the front meniscus interface, which increases local surfactant concentration and thus the overall pressure drop across the plug (Fujioka 2005). The resultant Marangoni stress yields nearly zero surface velocity opposite to the flow, and reduces the interface mobility through stiffening the precursor film (Fujioka 2005; Muradoglu 2019). Surfactant reduces surface tension and thus may reduce the risk of cell damage (Zheng 2007; Fujioka 2008; Muradoglu 2019).

Compared with Newtonian viscosity, the non-Newtonian effects of shear thinning reduce mucus deposition on airway walls (Laborie 2017), decrease mechanic forces imposed upon epithelial cells, and therefore lower the risk of epithelial cell damage (Zamankhan 2012 and 2018). The influence of yield stress is not as positive as that of shear thinning. Upon an increase of the yield stress, more mucus deposits along the airway walls (Laborie 2017), which, in turn, implies a higher risk of airway closure. Recent studies employed a Bingham model to take into account the yield stress effects of mucus and showed that high yield stress increases the gradients of wall shear stress and pressure, enhancing the damage of the epithelial cells (Zamankhan 2012 and 2018).

In a previous study, we experimentally investigated the mucus plug rupture in a collapsed lung airway of the 10^{th} generation by using a microfluidic model with carbopol gels as mucus simulant (Hu 2015). Our experiments showed near rupture appear rapid changes in shear stress and plug-shortening velocity. The dimensionless time-averaged shear stress linearly increases with the Bingham number (i.e. the ratio of yield stress to pressure difference). Crackling sounds, produced with rupture and closely related to mechanical stresses (Grotberg 2019), might be more detectable for mucus plugs with higher yield stress. In general, however, due to complex properties related to mucus, mucus plug rupture has not been completely understood. There even have been no reliable methods to measure mucus-air surface tension. Complementing our previous experiments, we focus on two mucus-related properties, surface tension and yield stress, to investigate their effects on mucus plug rupture by using a simplified airway model. Other properties and conditions remain fixed, such as the pressure difference across the mucus plug, the initial plug length and channel dimensions.

2 Method

Figure 1(a) depicts the sketch of our model which consists of a mucus plug in a channel. The channel is 1.5 mm (2*a*) wide, 0.12 mm (*h*) deep and 10 mm (*l*) long, similar to that used in our experiments (Hu 2015), except for the length (50 mm in the experiments). In the following, the two walls normal to the *y*-axis are called the *y*-walls, or front (*y*=0) and back (*y*=2*a*) walls, whereas the two walls normal to the *z*-axis are termed the *z*-walls, or bottom (*z*=0) and top (*z*=*h*) walls. The cross-sections at *x*=0 and *l* are inlet and outlet, respectively. The plug length is measured at the throat, i.e. the thinnest part of the plug along the central line (*y*=*a*, *z*=0.5*h*).

The initial shape and location of the plug in the channel is shown in Fig. 1(b). The plug is attached to the walls and is delimited by a planar surface at $x=0.2l+L_0$ and a half cylindrical surface with the axis located along *z* at $x=0.2l-a$ and $y=a$. Imposing a high pressure, p_0, at inlet and setting atmospheric pressure, p_a, at the outlet, we generate a pressure difference across the plug. If the pressure difference is large enough, the plug is pushed to move in the *x*-direction, deforms, and finally ruptures.

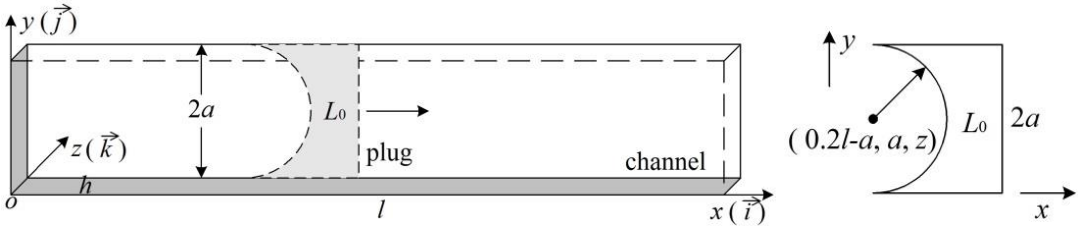

(a) (b)

Fig. 1 (a) The sketch of the channel with a mucus plug mounted. Channel length: $0\le x\le l$, width: $0\le y\le 2a$, and depth: $0\le z\le h$. L_0: initial plug length. $\vec{i}$, $\vec{j}$ and $\vec{k}$: unit normal vectors along *x*, *y* and *z*. (b) Top view of the initial shape and location of the plug in the channel.

2.1 Physical model

2.1.1 Governing equations

We suppose the flow is incompressible and laminar. Within each phase, the fluid flow is governed by the following continuity and momentum equations

$$\nabla\cdot\vec{V}_\alpha=0, \tag{1}$$

$$\rho_\alpha\frac{D\vec{V}_\alpha}{Dt}=-\nabla p_\alpha+\nabla\cdot\vec{\vec{\tau}}_\alpha+\vec{F}_\alpha, \tag{2}$$

where $\vec{V}_\alpha$ is the velocity vector, p_α the pressure field, $\vec{\vec{\tau}}_\alpha$ the shear stress tensor, ρ_α the density, and $\vec{F}_\alpha$ the source term due to the surface tension force exchanged across the interface between the two fluid phases, i.e. mucus and air. The subscript α indicates that Eqs. (1) and (2) are solved for both phases, air ($\alpha=a$) and mucus ($\alpha=m$).

The continuum surface stress model, in favor of conservation of the surface tension force, is used to calculate $\vec{F}_\alpha$ (Lafaurie 1994),

$$\vec{F}_\alpha=\nabla\cdot\vec{\vec{T}},\quad \vec{\vec{T}}=\sigma\left(|\nabla f|\vec{\vec{I}}-\frac{\nabla f\otimes\nabla f}{|\nabla f|}\right), \tag{3}$$

in which $\vec{\vec{I}}$ is the unit tensor, σ the surface tension, $\otimes$ the gradient tensor product, and *f* the volume fraction function valued between 0 (air) and 1 (mucus).

The conservation equation for f reads

$$\frac{Df}{Dt}=0\,. \tag{4}$$

It is noticed that the interfacial stress in Eq. (3) is valid in the limit in which the interface thickness vanishes, and ∇f can be interpreted as a delta-function (Lafaurie 1994). To avoid unacceptable numerical diffusion of the interface when directly discretizing and numerically solving Eq. (4), we use the volume of fluid (VOF) method, a geometric reconstruction scheme, to solve f and track plug deformation, in which the interface is approximated by a plane in a cell and the interface slope (i.e. ∇f) is determined by the f-value of the concerned interface cell and its twenty-six neighbor cells (Youngs 1982).

For the air, $\nabla\cdot\vec{\vec{\tau}}_a=\mu_a\nabla^2\vec{V}$, where μ_a is the dynamic viscosity of air. For mucus, the Herschel-Bulkley (HB) model characterizes the mucus plug's viscosity as follows (Bird 1983),

$$\begin{cases}\dot{\gamma}<\dot{\gamma}_c:\ \ \mu_m=\dfrac{\tau_0}{\dot{\gamma}_c}\left(2-\dfrac{\dot{\gamma}}{\dot{\gamma}_c}\right)+k\left[(2-n)+(n-1)\dfrac{\dot{\gamma}}{\dot{\gamma}_c}\right]\\ \dot{\gamma}\geq\dot{\gamma}_c:\ \ \mu_m=\dfrac{\tau_0}{\dot{\gamma}}+k\left(\dfrac{\dot{\gamma}}{\dot{\gamma}_c}\right)^{n-1}\end{cases}, \tag{5}$$

where $\dot{\gamma}$ is the second variant of the strain rate tensor, $\vec{\vec{D}}=\nabla\vec{V}+(\nabla\vec{V})^T$, and defined as $\dot{\gamma}=\sqrt{\frac{1}{2}\vec{\vec{D}}:\vec{\vec{D}}}$, $\dot{\gamma}_c$ the sensitive strain rate, k the consistency factor, and n the power-law index. Thus the shear stress of the mucus phase is written as $\vec{\vec{\tau}}_m=\mu_m\vec{\vec{D}}$. Here we use the carbopol gel at the concentration of 0.15% employed in our experiments, τ_0=33.0 Pa, n=0.545, k=28.86 Pa·s and $\dot{\gamma}_c$ =0.12 s^{-1}, to simulate physiologically-relevant conditions (Hu 2015).

2.1.2 Boundary and initial conditions

We set pressure-inlet and pressure-outlet conditions at the inlet and outlet of the channel, respectively, and no-slip all over the walls,

Inlet: $p=p_0$, $\vec{V}=u_{in}\vec{i}$,

Outlet: $p=p_a$ ($<p_0$), $\vec{V}=u_{out}\vec{i}$,

Walls: $\vec{V}_{wall}=0$,

where u_{in} (>0) and u_{out} are the unknown x-velocity components at the inlet and outlet, respectively. They are calculated by using the Bernoulli equation. The continuity and momentum equations are also involved for physical conservation and numerical convergence (ANSYS 2012). Considering that the flow in the entire domain is rather weak before rupture and the pressure drop over the air phase is thus negligible, we suppose p_0-p_a (>0) as the pressure difference, Δp, applied between the two interfaces of the mucus plug.

The surface stress model given in expression (3) and the surface conservation equation (4) serve as the dynamic and kinematic conditions on the mucus-air interface.

Initially, the mucus plug-air system is at rest and in normal atmospheric conditions.

2.1.3 Parameters and scaling

The mucus plug rupture is a function of mucus-related properties (yield stress, τ_0, viscosity, μ_m, surface tension, σ, and density, ρ_m), dimensions of the plug and the channel (initial plug length, L_0, the

half channel width, a, and channel depth, h), and the external driving-force (the pressure difference, Δp). That is,

$$\mathcal{F}(\tau_0, \mu_m, \sigma, \rho_m, L_0, a, h, \Delta p) = 0.$$

Choosing Δp, a and ρ_m as basic variables, it yields five dimensionless parameters,

$$\pi_1 = \frac{\tau_0}{\Delta p},\ \pi_2 = \frac{\sigma}{\Delta p a},\ \pi_3 = \frac{\sqrt{\Delta p \rho_m a^2}}{\mu_m},\ \pi_4 = \frac{L_0}{a} \text{ and } \pi_5 = \frac{h}{a}.$$

The first three non-dimensional groups, π_1 to π_3, involve mucus properties. The fourth one, π_4, considers the plug dimension, scaling the initial plug length on the half-height of the channel, and re-denoted as $\Lambda_{L0}=L_0/a$. The last one, π_5, is the spanwise aspect ratio, and re-denoted as $\lambda=h/a$. Based on Poiseuille flow, we define the characteristic velocity as $U=\Delta p a^2/(\mu_m L_0)=\Delta p a/(\mu_m \Lambda_{L0})$. Using the characteristic velocity, we re-define the first three dimensionless parameters above, the Bingham number, *Bn*, the capillary number (ratio of inertia to surface tension terms), *Ca*, and the Reynolds number (ratio of inertia to viscous terms), *Re*, as

$$Bn = \frac{\tau_0}{\mu_m U / a} = \Lambda_{L0} \frac{\tau_0}{\Delta p},\ Ca = \frac{\mu_m U}{\sigma} = \frac{\Delta p a}{\sigma \Lambda_{L0}} \text{ and } \mathrm{Re} = \frac{\rho_m U a}{\mu_m} = \frac{\rho_m \Delta p a^2}{\mu_m^2 \Lambda_{L0}},$$

which, in certain combinations of π_1 to π_4, are equivalent to the π-variables themselves, $Bn=\pi_1\pi_4$, $Ca=(\pi_2\pi_4)^{-1}$ and $Re=\pi_3^2/\pi_4$. To investigate the relation between yield stress and surface tension, we introduce their ratio, i.e. the ratio of the yield stress to the characteristic Laplace pressure,

$$\Pi = \frac{\tau_0}{\sigma / a} = Bn \cdot Ca \left(= \frac{\pi_1}{\pi_2} \right).$$

The wall shear stresses (WSSes), $\tau_{w.y}=\mu_m (\partial u/\partial y+\partial v/\partial x)$ and $\tau_{w.z}=\mu_m (\partial u/\partial z+\partial w/\partial x)$ on the y- and z-walls, are scaled by $\mu_m U/a=\Delta p/\Lambda_{L0}$, and denoted by the symbols, $T_{w.y}$ and $T_{w.z}$, respectively.

The focus of the current study is on the effects of surface tension and yield stress, corresponding to the two dimensionless parameters, *Bn* and *Ca*, respectively. For the HB mucus, the viscosity effects may not be dominant during the plug rupture process. We have used the Bingham fluid model (letting n=1 in the HB-model expression (5)) to estimate the effects of the yield stress dependence of viscosity. As a quick approximation, we take k as μ_m in the *Re*-definition. When k rises from 0.01 to 3.0 Pa·s and *Re* drops by five orders of magnitude from 1.7×10^4 to 0.2, the maximum wall shear stress (mWSS) on z-walls grows slightly from 1500 to 2800 Pa. We thus do not investigate further the effects of mucus viscosity in this study.

The other parameters are fixed. The values of the two dimensionless parameters about the plug and channel dimensions are $\Lambda_{L0}=\frac{0.5\,\mathrm{mm}}{0.75\,\mathrm{mm}}=0.667$ and $\lambda=\frac{0.12\,\mathrm{mm}}{0.75\,\mathrm{mm}}=0.16$. The pressure difference is Δp=2000 Pa. The mucus approximates the 0.15%-carbopol gel employed in the experiments of Hu et al (2015), except for the variation in yield stress. We change τ_0 from 0.03 to 100 Pa, i.e. $1.0\times10^{-5}\le Bn\le3.3\times10^{-2}$, to study the effects of yield stress. Surface tension σ varies within 1.0×10^{-4}~8.0×10^{-2} N/m, and correspondingly, *Ca* within 28.0~2.3×10^4. As a reference value for the mucus yield stress, we take τ_0=33.0 Pa (Hu 2015). The pressure difference on mucus in the 10^{th} generation is supposed to be 2000 Pa (Hu 2014; Henderson 2017; Umbrello 2017). The radius of the airway in the 10^{th} generation is ~0.5 mm, and the initial plug length relative to the airway radius is ~1. Thus, for physiologically-relevant mucus plugs in the human airways, $Bn\approx0.0165$, which falls in the range of the Bingham numbers considered in the current study. Moreover, the setting of $Ca\sim100$ at the surface tension $\sigma\sim0.01$ N/m is also within the studied range of capillary

numbers. The baseline case is defined with the parameters similar to those in the real lung airway conditions above, except that the initial plug length is L_0/a = 0.667 ($2a$ = 1.5 mm).

Finally, we define several time quantities which will be used in the following to analyze the simulation results:

t_r: total time needed for the plug to rupture with length reducing from the initial, L_0, to zero at rupture. The moment that Δp is applied on the plug to initiate the rupture process is taken as t=0.

$t_{L.5}$: time needed for the plug to reduce its length from L_0 to $0.5L_0$.

$t_{Tw.5}$: time needed for the instant greatest WSS to reach half-mWSS at rupture.

$t'_{L.5}=1-t_{L.5}/t_r$: ratio of the time needed for the plug to reduce its length from $0.5L_0$ to zero, relative to the total rupture time.

$t'_{Tw.5}=1-t_{Tw.5}/t_r$: ratio of the time needed for the plug to raise its WSS from half-mWSS to the final mWSS at rupture, relative to the total rupture time.

2.2 Numerical methods

The software package of computational fluid dynamics, ANSYS FLUENT®, is employed to carry out the simulations, performed on a desktop computer with Intel® Xeon® 3.4 GHz-CPU, 32.0 GB-RAM, and 64-bit Windows 7 Pro. The momentum equations are discretized using a 2nd-order upwind scheme. The conservation equation for the volume fraction function is solved using Geo-reconstruct. The PISO (pressure-implicit with splitting of operations) scheme is chosen as the velocity-pressure coupling method. PRESTO (pressure staggering option) is used for pressure iteration (ANSYS 2012).

The channel domain is meshed uniformly by 500 (N_x), 150 (N_y) and 20 (N_z) cells in length, width and depth, respectively, which grid is used throughout and named N_0. The time step of each calculation is fixed between 1.0×10^{-6} and 1.0×10^{-5} s depending on the simulation. The computation terminates when the plug ruptures.

We choose six more meshes, $0.5N_x\times N_y\times N_z$ (named $0.5N_x$), $N_x\times0.5N_y\times N_z$ ($0.5N_y$), $N_x\times N_y\times0.5N_z$ ($0.5N_z$), $2.0N_x\times N_y\times N_z$ ($2.0N_x$), $N_x\times2.0N_y\times N_z$ ($2.0N_y$) and $N_x\times N_y\times2.0N_z$ ($2.0N_z$), together with N_0, to investigate grid convergence of our results. For each mesh setting, we calculate the absolute error of a concerned quantity relative to the corresponding average from all of the seven mesh settings. Suppose φ_β (β=1, 2, ···, 7) is the quantity of interest obtained from the seven mesh settings, respectively, and $\overline{\varphi}$ is their average. Then the absolute relative error of the quantity obtained from one mesh setting is calculated as $\varepsilon_\beta=\left|\varphi_\beta/\overline{\varphi}-1\right|\times100\%$ (β=1, 2, ···, 7). Here we investigate ε_β-performance of three quantities, $t'_{L.5}$, $\tau_{w.z.max}$ and $\tau_{w.y.max}$, in each mesh setting. Figure 2 shows the mesh settings of N_0, $2.0N_y$ and $0.5N_z$ are better for the three quantities aforementioned, respectively. Considering numerical results with current computation capacity, we finally select N_0, 500×150×20, as the mesh setting.

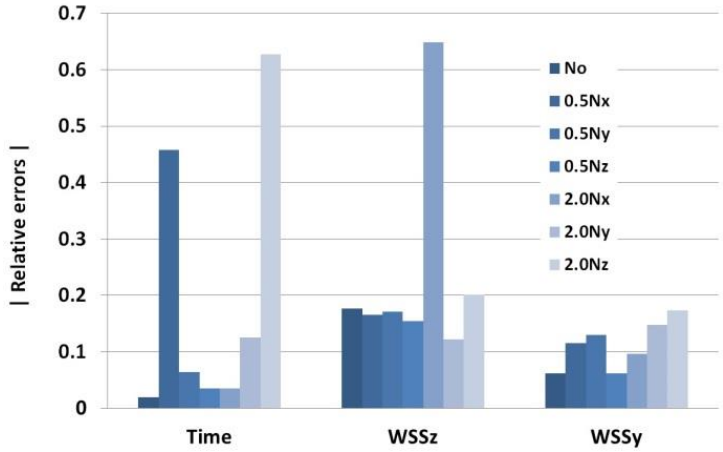

Fig. 2 The absolute values of the relative errors of Time ($t'_{L.5}$), WSSz ($\tau_{w.z.max}$) and WSSy ($\tau_{w.y.max}$), for seven mesh settings, N_0, $0.5N_x$, $0.5N_y$, $0.5N_z$, $2.0N_x$, $2.0N_y$ and $2.0N_z$.

3 Results

3.1 Rupture process

Figure 3 shows the distributions of pressure and velocity, and the mucus plug shape for the baseline case over different plane sections at several instants of time. The rupture occurs at t_r=0.143 s. The pressure difference is approximately applied across the plug because the pressure is almost uniform inside the air phase, separated by the plug (Figs. 3(a) and 3(b)). The velocity is generally aligned with the preferential direction of the pressure drop (Figs. 3(a) and 3(b)), except around the plug, especially near the central meniscus, where the velocity varies significantly in both magnitude and direction. At rupture, the velocity approaches its maximum at the broken meniscus. Due to the no-slip condition along the walls, mucus is deposited over the walls after the plug ruptures from the center (Figs. 3(c) and 3(d)).

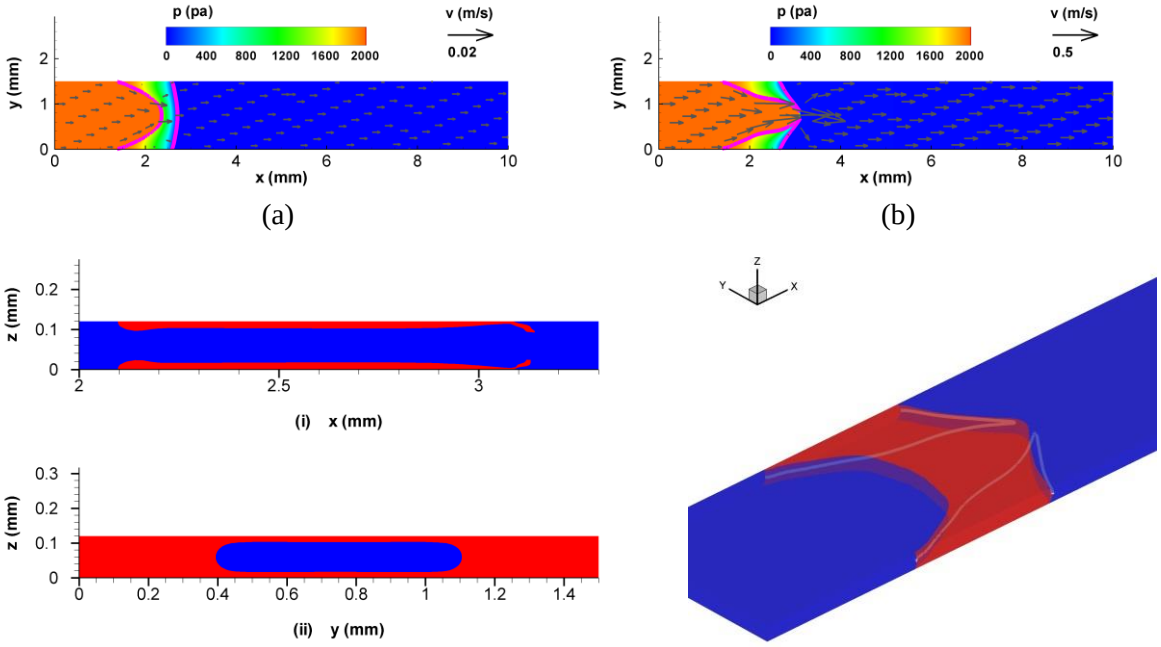

Fig. 3 On the plane section of z=0.5h, pressure and velocity fields are depicted together with the plug shape (solid lines) at t= (a) 0.7t_r and (b) t_r. At rupture, the plug shape is shown over the planes at (c-i) y=a,

(c-ii) x=0.25l, (d) z=0.5h (solid lines), and (d) in three dimensions. The initial plug length is L_0=0.5 mm, mucus-air surface tension σ=0.01 N/m, and the pressure difference Δp=2000 Pa. The VOF contour level is set at f=0.5 to show the plug shapes.

Figure 4(a) shows the shear stress distributions at the front (y=0) and top (z=h) walls at rupture. The high shear stress is located on the central line of each wall. The maximum WSS on the z-walls, $\tau_{w.max}$=1964.0 Pa (Fig. 4(a-i)), is more than six times the highest WSS on the y-walls, 306.1 Pa (Fig. 4(a-ii)). Figures 4(b-i) and 4(b-ii) show the unyielded regions ($\tau < \tau_0$, shaded areas) on the top wall (z=h) and the middle cross-section (z=0.5h), respectively, at rupture.

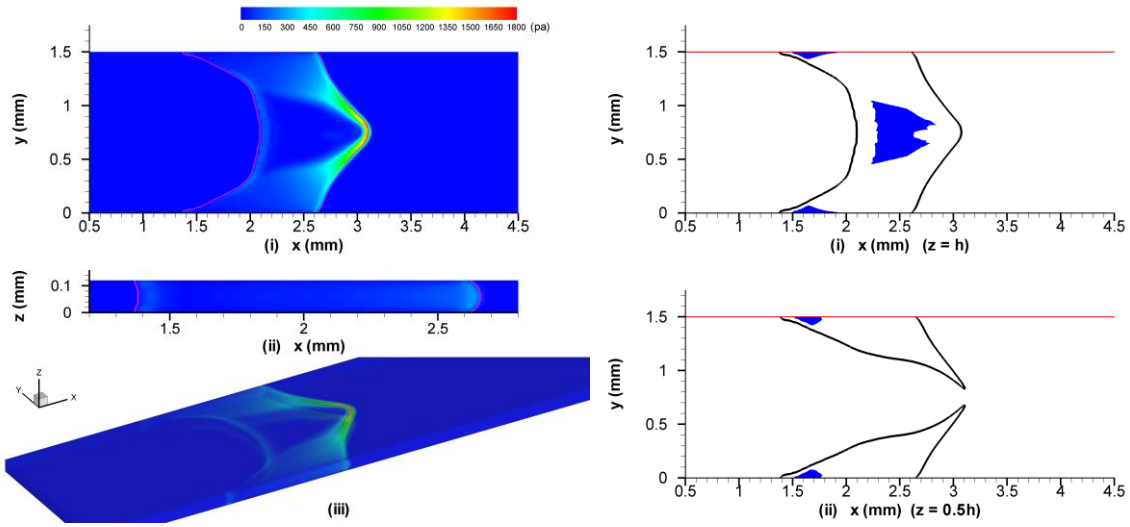

(a) (b)

Fig. 4 (a) At the rupture instant, the shear stress distributions on (a-i) the top wall, z=h, (a-ii) the front wall, y=0, and (a-iii) all the walls in three dimensions. (b) The unyielded regions of the plug (b-i) on the top wall, z=h, and (b-ii) on the middle cross-section, z=0.5h (depicted by the shaded areas). The solid lines (f=0.5) outline the plug shapes. The initial plug length is L_0=0.5 mm, mucus-air surface tension σ=0.01 N/m, and the pressure difference Δp=2000 Pa.

Figure 5 shows the history of the plug length shortening and the high shear stresses increasing at the y-/z-walls until rupture. In most of the process, about 90 percent, especially at the early stage, the plug deforms and shortens slowly. The dramatic change happens in a short period of time near rupture, say, from 0.9t_r to t_r. The maximum plug-shortening velocity magnitude, $v_{l.r}$=25.3 mm/s, appears at rupture, to which the plug takes only the last 10% of t_r to jump from a speed as low as 0.2$v_{l.r}$. The value of $\tau_{w.z}$ increases by 2.5 folds to the maximum, $\tau_{w.max}$=1964.0 Pa, at rupture. We thus define the time interval, from 0.9t_r to t_r, as the $t_{r10\%}$-interval. Compared with $\tau_{w.z}$, $\tau_{w.y}$ has not only a small magnitude but also a much mild increment.

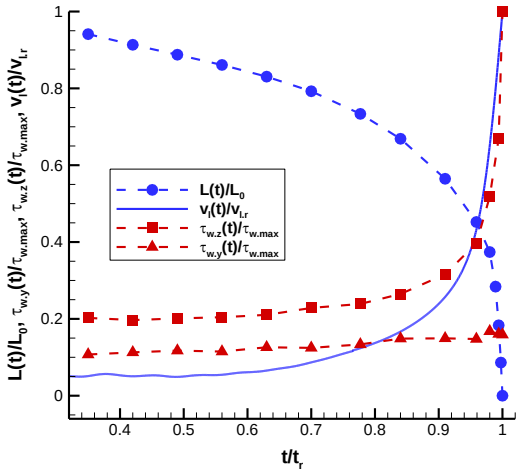

Fig. 5 With time vary the plug length, $L(t)/L_0$, velocity magnitude of the plug length shortening, $v_l(t)=v_{l.r}$, and the maximum shear stresses on the y-/z-walls, $\tau_{w.y}(t)/\tau_{w.max}$ and $\tau_{w.z}(t)/\tau_{w.max}$, in the plug rupture process. The plug here is the same as the one in Fig. 3. At rupture, the plug-shortening velocity magnitude is $v_{l.r}$=25.3 mm/s, and the mWSS is $\tau_{w.max}$=1964.0 Pa.

More plugs are studied to investigate how the magnitudes of surface tension and yield stress influence plug deformation, as shown in Fig. 6. The surface tension in Fig. 6(a-ii) is σ=0.1 N/m, 10^3 times that in Fig. 6(a-i). The yield stress in Fig. 6(b-ii), τ_0=100.0 Pa, is also 10^3 times that in Fig. 6(b-i). Except the magnitude difference in σ and τ in Figs. 6(a) and 6(b), respectively, the other parameters follow the baseline setup. With the higher surface tension, the plug deforms more smoothly and displays better extensibility, as shown in Fig. 6(a-ii). This is understood considering the resistance to rupture provided by an enhanced σ. Moreover, even though the yield stresses in Figs. 6(b-i) and 6(b-ii) differ by three orders of magnitude, the resultant deformation patterns are qualitatively very similar.

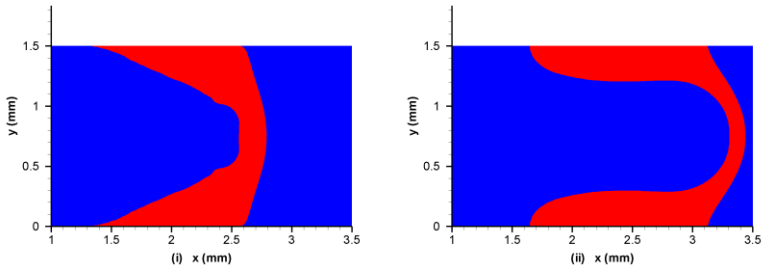

(a)

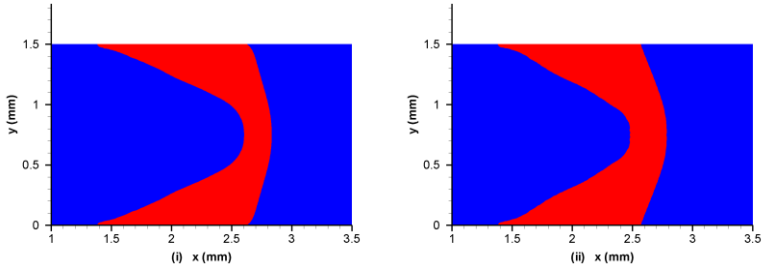

(b)

Fig. 6 The plug shapes on the plane section z=0.5h at 0.9t_r. (a-i) σ=1.0×10^{-4} N/m, (a-ii) σ=0.1 N/m, (b-i) τ_0=0.1 Pa, and (b-ii) τ_0=100.0 Pa. The other quantities are the same as those in the baseline case. The VOF contour level is set at f=0.5.

Figure 7 shows how t_r, $t_{L.5}$, $t_{Tw.5}$, $t'_{L.5}$ and $t'_{Tw.5}$ change depending on surface tension and yield stress. The dimensional times, t_r, $t_{L.5}$ and $t_{Tw.5}$, increase with the surface tension and the yield stress. Their growths are particularly pronounced when σ and τ_0 are greater than certain values, which we therefore define as sensitive values (by subscript s), σ_s=0.01 N/m (Fig. 7(a-i)) and τ_s=2.0 Pa (Fig. 7(b-i)). For the non-dimensional time, $t'_{L.5}$, it experiences a sharp drop from a high, almost constant value to a low plateau when Ca_s≈100, as denoted in Fig. 7(a-ii). The dimensionless time ratio in Fig. 7(a-ii), $t'_{Tw.5}$, drops around Ca_s as well from the peak of 0.36 to a plateau at 0.015 after rising with Ca. With Bn rising, $t'_{L.5}$ remains nearly constant, $t'_{L.5}$≈0.15, until it rapidly decades around Bn_s=0.01, as shown in Fig. 7(b-ii). The trend of $t'_{Tw.5}$ in Fig. 7(b-ii) is smooth and slightly drops upon an increase of Bn, except for a small peak around Bn_s, which is about four times its valley neighbors.

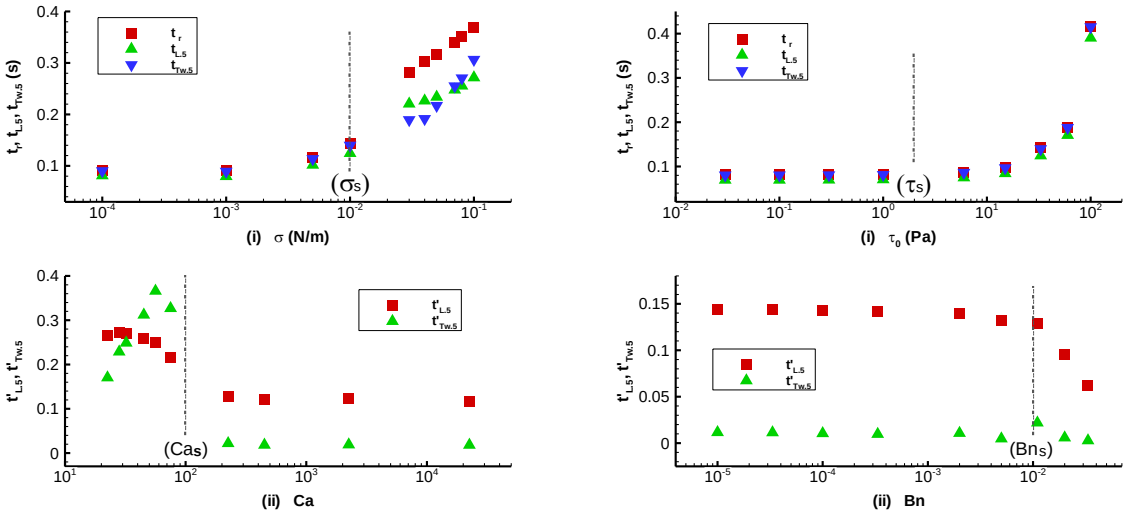

(a) (b)

Fig. 7 Time variables, t_r, $t_{L.5}$, $t_{Tw.5}$, $t'_{L.5}$ and $t'_{Tw.5}$, vary with (a) surface tension, σ, and Ca (at Bn=0.011), and (b) yield stress, τ_0, and Bn (at Ca=225.0).

We also plot the time ratios, $t'_{L.5}$ and $t'_{Tw.5}$, in terms of Π (=Bn·Ca) under various conditions, as shown in Fig. 8. The time ratios are strongly Π-dependent around Π~O(1). We take $-1<\log\Pi<1$, exponentially symmetric about the specified value of $\log\Pi_s$=0, i.e. Π_s=1, hereinafter as the sensitive zone, where the effects due to surface tension and yield stress are comparable. In the sensitive zone, both $t'_{L.5}$ and $t'_{Tw.5}$ vary in relatively large ranges, 0.06~0.3 (Fig. 8(a)) and 0.02~0.5 (Fig. 8(b)), respectively. Out of this zone, $t'_{L.5}$ and $t'_{Tw.5}$ vary moderately. With Π increasing, $t'_{L.5}$ somewhat decreases from 0.15 to 0.14 (Fig. 8(a)), and $t'_{Tw.5}$ increases from 0.01 to 0.02 (Fig. 8(b)).

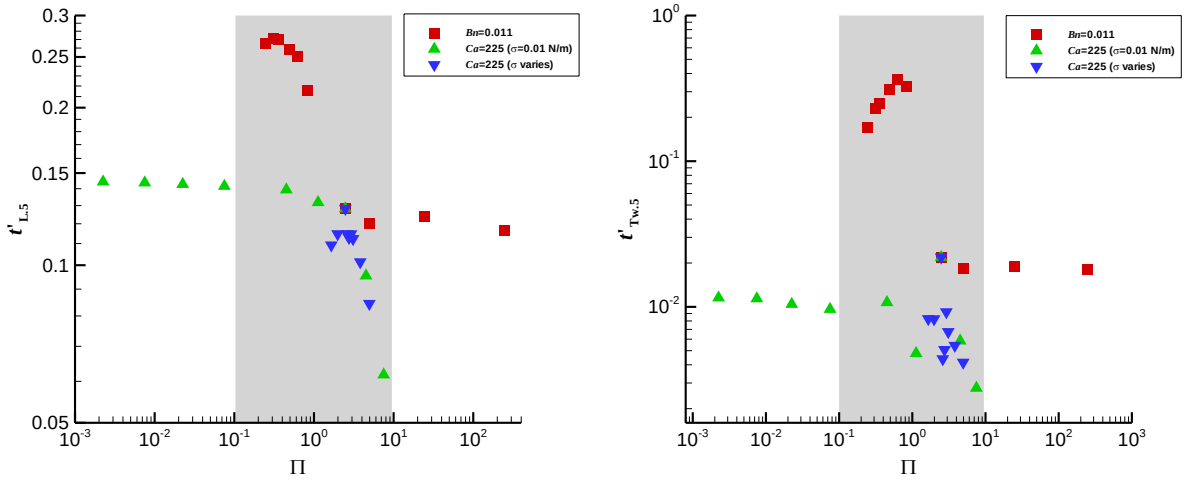

Fig. 8 The time ratios, (a) $t'_{L.5}$ and (b) $t'_{Tw.5}$, change with Π. The greyed areas, $-1<\log\Pi<1$, indicate the sensitive zones, where the data are strongly Π-dependent.

3.2 Wall shear stress

To investigate the effects of surface tension on WSS, we change only the surface tension within $1.0\times10^{-4}<\sigma<0.1$ N/m, and keep the other parameters consistent with the baseline case. Generally, a higher surface tension results in higher WSSes, $\tau_{w.z}$ and $\tau_{w.y}$, which are more pronounced at $\sigma>\sigma_s$, as shown in Fig. 9(a-i). Similar to the effects of surface tension in Fig. 7(a-i), the WSSes, especially $\tau_{w.z}$, fluctuate when $\sigma\approx\sigma_s$. At small σ, the magnitude of $\tau_{w.z}$ can be as high as eight times $\tau_{w.y}$. When σ increases, however, the ratio, $\tau_{w.z}/\tau_{w.y}$, gradually diminishes until $\tau_{w.z}/\tau_{w.y}\approx2$ when $\sigma\approx\sigma_s$ (Fig. 9(a-i)). In non-dimensions, $T_{w.z}$ and $T_{w.y}$ decrease with Ca and experience some fluctuations around Ca_s, as shown in Fig. 9(a-ii), together with a rapid decrease when $Ca<Ca_s$.

In Fig. 9(b), we change only the yield stress within the range, $0.03<\tau_0<100$ Pa. The WSS magnitudes, both in dimensions and non-dimensions, together with the WSS-ratio, seem to experience no significant change when τ_0 and Bn increase, except for some fluctuations observed when $\tau_0\approx\tau_s$ (Fig. 9(b-i)) and $Bn\approx Bn_s$ (Fig. 9(b-ii)).

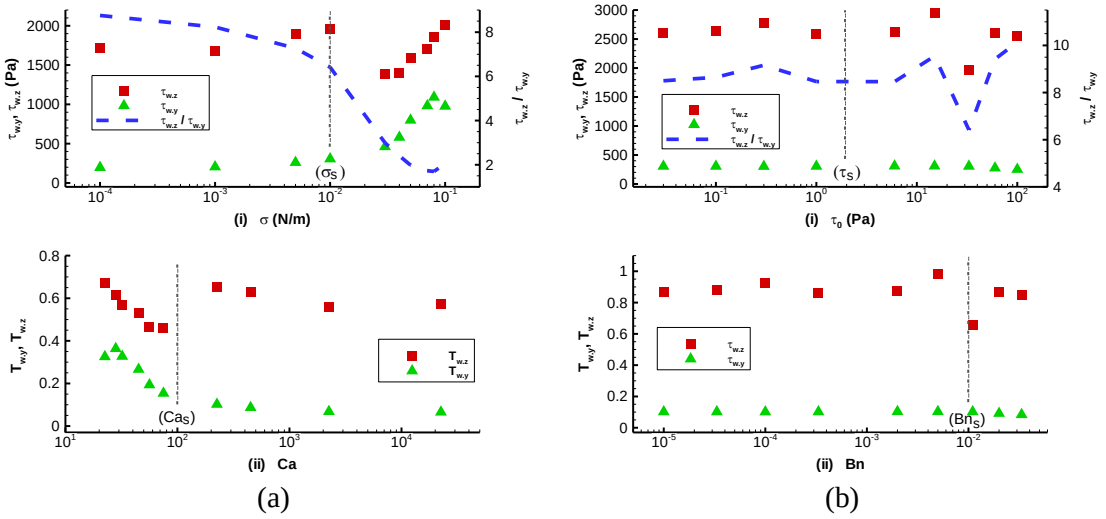

Fig. 9 Dimensional and non-dimensional WSSes vary with (a) the surface tension, σ, and Ca (at Bn=0.011), and (b) the yield stress, τ_0, and Bn (at Ca=225.0). The dashed lines in (a-i) and (b-i) indicate the WSS-ratio, $\tau_{w.z}/\tau_{w.y}$, in terms of σ and τ_0, respectively.

Both $T_{w.z}$ and $T_{w.y}$ fluctuate dramatically in the sensitive zone ($-1<\log\Pi<1$), ranging within $0.46<T_{w.z}<1.04$ and $0.065<T_{w.y}<0.36$, respectively, as shown in Fig. 10. Out of the sensitive zone for Π, the two WSSes are nearly constant; upon an increase of Π in the sensitive zone, $T_{w.z}$ drops from about 0.9 to 0.6, and $T_{w.y}$ from 0.1 to 0.065.

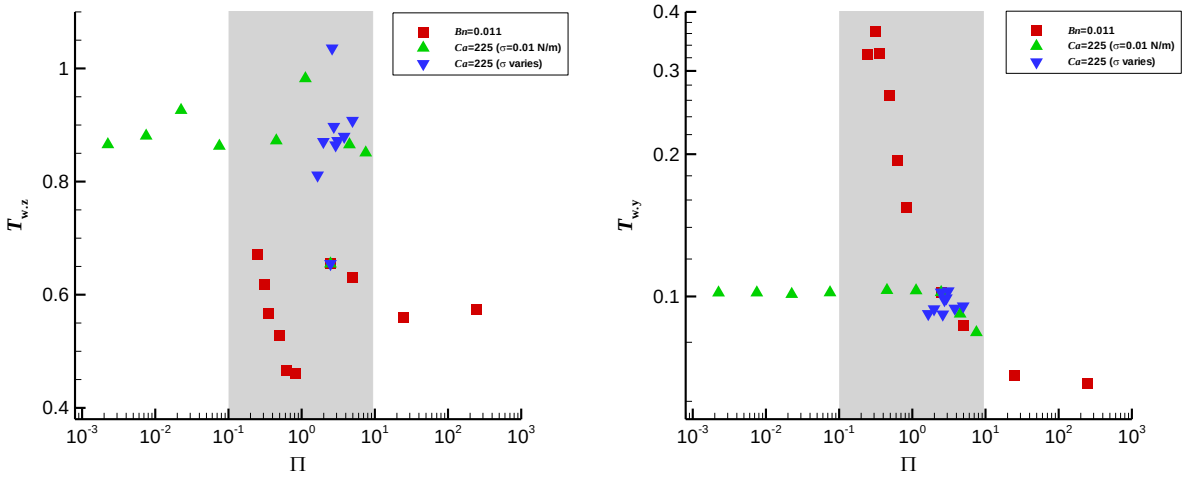

Fig. 10 Non-dimensional WSSes, (a) $T_{w.z}$ and (b) $T_{w.y}$, vary with Π. The greyed areas, $-1<\log\Pi<1$, i.e. the sensitive zones, indicate where the data are strongly Π-dependent.

4 Discussion

4.1 Rupture process

The two mucus-related properties, surface tension and yield stress, both oppose to plug rupture, but follow different physical mechanisms. The surface tension effects depend on plug curvature, i.e. they are geometry-dependent, whereas the yield stress effects are geometry independent. Initially, the plug deformation is small, and the yield force is the primary resistance the plug needs to overcome to deform. With the plug overcoming the yield force, moving as a real fluid and continuously deforming, the surface tension effects gradually overtake the yield stress. At a later stage, the plug deforms greatly up to breaking up, experiencing large curvatures, and the surface tension effects become significant. Thus the surface tension and yield forces take turns to resist during the rupture process.

Significant flow changes appear around the plug, especially at the plug meniscus location, right prior to rupture (Figs. 3 and 4). The velocity varies abruptly in both magnitude and direction. The rupture even leads to a jet through the broken plug meniscus (Fig. 3(b)). The mWSS occurs on the z-walls where the plug meniscus tip is located (Fig. 4). The plug is the major bearer of the pressure difference between the inlet high and the outlet low pressure regions. The pressure distributes almost uniformly in the air either behind or ahead of the plug (Figs. 3(a) and 3(b)), which justifies the approximation used in the study that the pressure difference across the plug is the same as that measured between the inlet and outlet. The unyielded parts of the plug are around the walls (Fig. 4(b)), which is different from what observed for Newtonian fluid flows that at walls often appears great shear stress.

The most dramatic changes for the fluid flow occur in the $t_{r10\%}$-interval (Fig. 5). With the plug length being quickly shortened, the curvature grows fast; WSS increases synchronously and reaches the maximum at the rupture instant.

The magnitude of the surface tension in Fig. 6(a-ii), two-order higher than that in Fig. 6(a-i), is the reason that the plug appears more extensible since a higher interfacial resistance is provided by σ. By comparison, the plug deformations in Figs. 6(b-i) and 6(b-ii) look similar, though their yield stresses differ by three orders of magnitude.

Large surface tension slows down the rupture process (Fig. 7(a-i)). The plug deformation induced by the pressure difference leads to interfacial energy growth. Surface tension tends to establish an equilibrium condition to minimize surface energy, and therefore opposes the plug deformation and resists plug rupture. The resistance is greater at the larger surface tension. Since the driving force of the pressure difference does not change in this study, the development of the plug deformation is slowed down and the rupture process is extended. Similar is the reason of the slowdown of the rupture process at large yield stress (Fig. 7(b-i)) because increased yield stress also raises the resistance on the plug. However, the two resistance forces dominate different stages of the rupture process. A plug at large surface tension ($\sigma > \sigma_s$) has high extensibility (Fig. 7(a-i)). The clear difference between t_r and $t_{L.5}$ (or $t_{Tw.5}$) indicates that surface tension has more influence on the later stage of the rupture process rather than at the beginning. By comparison, the three time values grow pretty consistently with yield stress increasing and t_r is only slightly larger than $t_{L.5}$ (or $t_{Tw.5}$) (Fig. 7(b-i)), so the yield stress plays an important role mainly at the early stage of the rupture process.

Distinct influence from surface tension and yield stress is further seen on the relative time quantity, $t'_{L.5}$ (indicating how fast the plug shortens at the late stage). Great plug extensibility due to large surface tension is especially pronounced at the late stage. The plug may deform for a relatively long time before rupture, as we see that $t'_{L.5}$ increases with Ca decreasing (Fig. 7(a-ii)). By contrast, the plug extension granted by the yield stress resistance mainly has an effect at the early stage of the plug deformation. The plug takes longer time to overcome a higher yield stress, so $t'_{L.5}$ decreases with yield stress (i.e., increasing Bn in Fig. 7(b-ii)).

The quantity, $t'_{Tw.5}$, measures how relatively fast WSS develops in the late rupture process. At $Ca < Ca_s$, i.e. $\sigma > \sigma_s$, high surface tension improves plug deformability, postpones appearances of both half mWSS and mWSS, and widens their interval relative to the whole process (Fig. 7(a)). This implies that great deformability may decelerate the development of the plug deformation strain, since mWSS—essentially shear stress—is a function of the strain rate, and not of the strain itself. With regard to yield stress, after yielding, the mucus behaves as a fluid and the yield stress effects are no more easily singled out. Variation in $t'_{Tw.5}$ due to yield stress change is negligible (Fig. 7(b-ii)). The slight drop in $t'_{Tw.5}$ with Bn increasing is an evidence that yield stress, effective in the early period and thus extending the entire process, has little influence on plug physics in the late period of the plug rupture.

Another observation is that the effects of surface tension and yield stress seem sensitive to certain values, σ_s=0.01 N/m and τ_s=2.0 Pa (corresponding to the dimensionless sensitive parameters, Ca_s=100 and Bn_s=0.01, respectively), beyond which the plug takes much more time to rupture (Fig. 7). Since the surface tension and yield forces take over the rupture process separately, the former during the final phase and the latter at the beginning, there should exist a time interval during which the two forces are comparable and tie. As predicted and shown in Fig. 8, the magnitudes of $t'_{L.5}$ and $t'_{Tw.5}$ strongly depend on the ratio of the two forces when they are comparable.

4.2 Wall shear stress

Both WSS and the surface tension effects are deformation-related and reach their maxima near rupture, while yield stress maintains quite constant, stable effects in the whole process. Therefore WSS seems sensitive to surface tension far more than yield stress (Fig. 9). WSS decays rapidly when $\sigma > \sigma_s$, as well as for $Ca < Ca_s$ (Fig. 9(a)), whereas variations in yield stress do not lead to a clear monotone trend of WSS which slightly fluctuates at $\tau_0 \approx \tau_s$ (i.e. $Bn \approx Bn_s$) (Fig. 9(b)).

The WSS is a function of the deformation strain rate of the plug. Geometrically, the plug deformation has two contributors, the channel spanwise aspect ratio and the plug itself. The large width-to-height aspect ratio of the rectangular channel cross-section leads to greater shearing of the plug on the *z*-walls than the *y*-walls, as the result, $\tau_{w.z} > \tau_{w.y}$, shows. This can be understood, at least partially, through the Newtonian Poiseuille flow with the same channel cross-section arrangement, in which the channel is the only geometric contributor and the WSS-ratio, $\tau_{w.z}/\tau_{w.y}$, is estimated to be 1.35. The plug rupture, much more complicated, usually yields a WSS-ratio larger than 2.0 (Figs. 9(a-i) and 9(b-i)). Since the extensibility of the plug increases upon an increase of the surface tension (Fig. 6(a)), it is expected that, at certain surface tension, the deformation contribution from the surface tension to the plug can exceed that from the fixed channel. Measured with mean curvature of a surface, the surface tension force has no orientation preference on plug deformation, and thus reduces the disparity of shearing on the two oriented channel walls. The resultant WSS-ratio therefore decreases with the rising surface tension (Fig. 9(a-i)). The WSS-ratio also shows sensitivity to σ_s, at which it rapidly drops. The effects of yield stress on the WSS-ratio are quite consistent when yield stress varies (Fig. 9(b-i)). This agrees with the discussion aforementioned that the yield stress effects play the major role at the beginning of the process, and keep constant in the whole process. Similar to WSS, the WSS-ratio is more sensitive to surface tension than to yield stress (Figs. 9(a-i) and 9(b-i)).

We here point out that the pressure difference, as the only driving force, has effects on the plug rupture far more than surface tension and yield stress. Even though WSS is sensitive to surface tension, the influence of surface tension on WSS is limited. In this study, *Ca* changes within $O(10^1) \sim O(10^4)$, so the role of the pressure difference is relatively advantageous. Compared with the three-order magnitude change of *Ca*, T_w remains of the same order, the maximum being about 1.5 times the minimum (Fig. 9(a-ii)). The pressure difference also overtakes yield stress, since the maximum Bingham number in this study, $Bn \sim O(10^{-2})$, is far less than 1.0. The magnitude of *Bn* also changes by three orders, but T_w is almost a constant of 0.864±0.094 (dimensionally 2587.1±264.4 Pa) (Fig. 9(b-ii)).

Figure 10 indicates, when the surface tension force is comparable with the yield force, the WSSes strongly depend on the ratio of the two forces. The baseline case, Δp=2000 Pa, σ=0.01 N/m, τ_0=33.0 Pa and following the HB model of the 0.15%-carbopol gel, is relevant to physiological conditions, and falls within the range that the surface tension effects have comparable importance to the yield stress effects. In this range, using surfactant to adjust the surface tension between mucus and air might be a very challenging control strategy.

4.3 Limitations

Considering the biologically-relevant scenarios in human lung airways, we limited the most important parameters of our study, such as the capillary number and the Bingham number, to certain ranges of the parameter space. Moreover, the effects of mucus viscosity on the plug rupture have not been fully investigated based on preliminary simulations. Comparing our results with literature studies (e.g. our previous research by Hu et al. (2015)) shows that the dimensions of the channel and of the plug have played an important role on rupture dynamics, which parameters, however, have not been investigated in this study. This study is therefore to be considered as a first insight into the effects of surface tension and yield stress for viscoplastic flows, and further simulations would help strengthen the conclusions drawn in

the following section. Due to the limited computation resources, the numerical accuracy could not be increased.

5 Conclusions

In this numerical study, we focus on the effects that surface tension and yield stress have on the rupture of a mucus plug in a model for a collapsed human lung airway. We come to the following findings:

- The maximum wall shear stress occurs at rupture, induced by the dramatically fast dynamics of the mucus plug.
- Since surface tension effects are curvature-dependent, surface tension influences mainly the late stage of the entire process when the plug deforms greatly to rupture. Upon an increase of surface tension, the plug extensibility grows postponing the rupture. Wall shear stress grows upon an increase in surface tension.
- Yield stress effects are important at the beginning when the pressure difference is applied to make the plug yield. High yield stress slows down the yielding of the plug, as well as the whole rupture process.
- When the surface tension and the yield stress induce comparable effects, the dynamical quantities are strongly dependent on the ratio of the surface tension and yield forces.
- Among the driving due to the pressure difference and the resistance due to surface tension and yield stress, the pressure difference contributes the most to the wall shear stress, and the yield stress offers the least significant contribution to the wall shear stress. The wall shear stress can be effectively reduced if the pressure difference, the surface tension, or both, are lowered.

6 Acknowledgements

The support of the NIH grant R01-HL136141 is kindly acknowledged.

References

1. ANSYS, 2012, "ANSYS 14.5 help," *Technical Report ANSYS Group*, ANSYS Inc., Canonsburg, PA, USA.
2. Bertram, C. and Gaver, D. P., 2005, "Biofluid mechanics of the pulmonary system," *Annals of Biomedical Engineering*, 33(12), pp. 1681-1688.
3. Bilek, A. M., Dee, K. C., and Gaver, D. P., 2003, "Mechanisms of surface-tension-induced epithelial cell damage in a model of pulmonary airway reopening," *Journal of Applied Physiology*, 94(2), pp. 770-783.
4. Bird, R. B., Dai, G. C., and Yarusso, B. J., 1983, "The rheology and flow of viscoplastic materials," *Reviews in Chemical Engineering*, 1(1), pp. 1-70.
5. Carnielli, V. P., Zimmermann, L. J. I., Hamvas, A., and Cogo, P. E., 2009, "Pulmonary surfactant kinetics of the newborn infant: novel insights from studies with stable isotopes," *Journal of Perinatology*, 29, pp. S29-S37.
6. Ducloue, L., Hazel, A. L., Thompson, A. B., and Juel, A., 2017, "Reopening modes of a collapsed elasto-rigid channel," *Journal of Fluid Mechanics*, 819, pp. 121-146.
7. Ellyett, K. M., Cragg, P. A., and Broadbent, R. S., 2006, "Effect of surfactant deficiency and surfactant replacement on airway patency in the piglet lung," *Respiratory Physiology & Neurobiology*, 150(2-3), pp. 173-181.
8. Fujioka, H. and Grotberg, J. B., 2004, "Steady propagation of a liquid plug in a two-dimensional channel," *Journal of Biomechanical Engineering Transactions of the ASME*, 126(5), pp. 567-577.

9. Fujioka, H. and Grotberg, J. B., 2005, "The steady propagation of a surfactant-laden liquid plug in a two-dimensional channel," *Physics of Fluids*, 17(0821028).
10. Fujioka, H., Takayama, S., and Grotberg, J. B., 2008, "Unsteady propagation of a liquid plug in a liquid-lined straight tube," *Physics of Fluids*, 20(0621046).
11. Grotberg, J. B., 2019, "Crackles and wheezes: agents of injury?" *Annals of the American Thoracic Society*, 16(8), pp. 967-969.
12. Halpern, D. and Grotberg, J. B., 1992, "Fluid-elastic instabilities of liquid-lined flexible tubes," *Journal of Fluid Mechanics*, 244, pp. 615-632.
13. Hassan, E. A., Uzgoren, E., Fujioka, H., Grotberg, J. B., and Shyy, W., 2011, "Adaptive Lagrangian-Eulerian computation of propagation and rupture of a liquid plug in a tube," *International Journal for Numerical Methods in Fluids*, 67(11), pp. 1373-1392.
14. Henderson, W. R., Chen, L., Amato, M., and Brochard, L. J., 2017, "Fifty years of research in ARDS. Respiratory mechanics in acute respiratory distress syndrome," *American Journal of Respiratory and Critical Care Medicine*, 196(7), pp. 822-833.
15. Hu, Y., Bian, S., Filoche, M., Grotberg, J. C., White, J., Takayama, S., and Grotberg, J. B., 2014, "Flow and sound generation in human lungs: Models of wheezes and crackles," In Zhou, Y., Liu, Y., Huang, L., and Hodges, D. H., editors, *Fluid-structure-sound interactions and control, Series: Lecture Notes in Mechanical Engineering 2014*, pp. 301-317, Berlin, Heidelberg. Springer Berlin Heidelberg.
16. Hu, Y., Bian, S., Grotberg, J., Filoche, M., White, J., Takayama, S., and Grotberg, J. B., 2015, "A microfluidic model to study fluid dynamics of mucus plug rupture in small lung airways," *Biomicrofluidics*, 9(0441194).
17. Huh, D., Fujioka, H., Tung, Y. C., Futai, N., Paine, R. R., Grotberg, J. B., and Takayama, S., 2007, "Acoustically detectable cellular-level lung injury induced by fluid mechanical stresses in microfluidic airway systems," *Proc Natl Acad Sci USA*, 104(48), pp. 18886-91.
18. Kay, S. S., Bilek, A. M., Dee, K. C., and Gaver, D. P., 2004, "Pressure gradient, not exposure duration, determines the extent of epithelial cell damage in a model of pulmonary airway reopening," *Journal of Applied Physiology*, 97(1), pp. 269-276.
19. Laborie, B., Rouyer, F., Angelescu, D. E., and Lorenceau, E., 2017, "Yield-stress fluid deposition in circular channels," *Journal of Fluid Mechanics*, 818, pp. 838-851.
20. Lafaurie, B., Nardone, C., Scardovelli, R., Zaleski, S., and Zanetti, G., 1994, "Modelling merging and fragmentation in multiphase flows with SURFER," *Journal of Computational Physics*, 113, pp. 134-147.
21. Magniez, J. C., Baudoin, M., Liu, C., and Zoueshtiagh, F., 2016, "Dynamics of liquid plugs in prewetted capillary tubes: from acceleration and rupture to deceleration and airway obstruction," *Soft Matter*, 12(42), pp. 8710-8717.
22. Mamba, S. S., Magniez, J. C., Zoueshtiagh, F., and Baudoin, M., 2018, "Dynamics of a liquid plug in a capillary tube under cyclic forcing: memory effects and airway reopening," *Journal of Fluid Mechanics*, 838, pp. 165-191.
23. Muradoglu, M., Romanò, F., Fujioka, H., and Grotberg, J. B., 2019, "Effects of surfactant on propagation and rupture of a liquid plug in a tube," *Journal of Fluid Mechanics*, 872, pp. 407-437.
24. Romanò, F., Fujioka, H., Muradoglu, M., and Grotberg, J. B., 2019, "Liquid plug formation in an airway closure model," *Physical Review Fluids*. (submitted).
25. Umbrello, M., Formenti, P., Bolgiaghi, L., and Chiumello, D., 2017, "Current concepts of ARDS: A narrative review," *International Journal of Molecular Sciences*, 18(64).

26. Willson, D. F. and Notter, R. H., 2011, "The future of exogenous surfactant therapy," *Respiratory Care*, 56(9), pp. 1369-1386.
27. Youngs, D. L., 1982, "Time dependent multi-material flow with large fluid distortion," In Morton, K. W. and Baines, M. J., editors, *Numerical Methods for Fluid Dynamics*, pp. 273-285. Academic Press.
28. Zamankhan, P., Helenbrook, B. T., Takayama, S., and Grotberg, J. B., 2012, "Steady motion of Bingham liquid plugs in two-dimensional channels," *Journal of Fluid Mechanics*, 705(SI), pp. 258-279.
29. Zamankhan, P., Takayama, S., and Grotberg, J. B., 2018, "Steady displacement of long gas bubbles in channels and tubes filled by a Bingham fluid," *Physical Review Fluids*, 3(0133021).
30. Zheng, Y., Fujioka, H., and Grotberg, J. B., 2007, "Effects of gravity, inertia, and surfactant on steady plug propagation in a two-dimensional channel," *Physics of Fluids*, 19(8), 082107.

Figure captions:

Fig. 1 (a) The sketch of the channel with a mucus plug mounted. Channel length: $0 \le x \le l$, width: $0 \le y \le 2a$, and depth: $0 \le z \le h$. L_0: initial plug length. $\vec{i}$, $\vec{j}$ and $\vec{k}$: unit normal vectors along x, y and z. (b) Top view of the initial shape and location of the plug in the channel.

Fig. 2 The absolute values of the relative errors of Time ($t'_{L.5}$), WSSz ($\tau_{w.z.max}$) and WSSy ($\tau_{w.y.max}$), for seven mesh settings, N_0, $0.5N_x$, $0.5N_y$, $0.5N_z$, $2.0N_x$, $2.0N_y$ and $2.0N_z$.

Fig. 3 On the plane section of $z=0.5h$, pressure and velocity fields are depicted together with the plug shape (solid lines) at $t=$ (a) $0.7t_r$ and (b) t_r. At rupture, the plug shape is shown over the planes at (c-i) $y=a$, (c-ii) $x=0.25l$, (d) $z=0.5h$ (solid lines), and (d) in three dimensions. The initial plug length is L_0=0.5 mm, mucus-air surface tension σ=0.01 N/m, and the pressure difference Δp=2000 Pa. The VOF contour level is set at f=0.5 to show the plug shapes.

Fig. 4 (a) At the rupture instant, the shear stress distributions on (a-i) the top wall, $z=h$, (a-ii) the front wall, $y=0$, and (a-iii) all the walls in three dimensions. (b) The unyielded regions of the plug (b-i) on the top wall, $z=h$, and (b-ii) on the middle cross-section, $z=0.5h$ (depicted by the shaded areas). The solid lines (f=0.5) outline the plug shapes. The initial plug length is L_0=0.5 mm, mucus-air surface tension σ=0.01 N/m, and the pressure difference Δp=2000 Pa.

Fig. 5 With time vary the plug length, $L(t)/L_0$, velocity magnitude of the plug length shortening, $v_l(t)=v_{l.r}$, and the maximum shear stresses on the y-/z-walls, $\tau_{w.y}(t)/\tau_{w.max}$ and $\tau_{w.z}(t)/\tau_{w.max}$, in the plug rupture process. The plug here is the same as the one in Fig. 3. At rupture, the plug-shortening velocity magnitude is $v_{l.r}$=25.3 mm/s, and the mWSS is $\tau_{w.max}$=1964.0 Pa.

Fig. 6 The plug shapes on the plane section $z=0.5h$ at $0.9t_r$. (a-i) $\sigma=1.0\times10^{-4}$ N/m, (a-ii) σ=0.1 N/m, (b-i) τ_0=0.1 Pa, and (b-ii) τ_0=100.0 Pa. The other quantities are the same as those in the baseline case. The VOF contour level is set at f=0.5.

Fig. 7 Time variables, t_r, $t_{L.5}$, $t_{Tw.5}$, $t'_{L.5}$ and $t'_{Tw.5}$, vary with (a) surface tension, σ, and Ca (at Bn=0.011), and (b) yield stress, τ_0, and Bn (at Ca=225.0).

Fig. 8 The time ratios, (a) $t'_{L.5}$ and (b) $t'_{Tw.5}$, change with Π. The greyed areas, $-1<\log\Pi<1$, indicate the sensitive zones, where the data are strongly Π-dependent.

Fig. 9 Dimensional and non-dimensional WSSes vary with (a) the surface tension, σ, and Ca (at Bn=0.011), and (b) the yield stress, τ_0, and Bn (at Ca=225.0). The dashed lines in (a-i) and (b-i) indicate the WSS-ratio, $\tau_{w.z}/\tau_{w.y}$, in terms of σ and τ_0, respectively.

Fig. 10 Non-dimensional WSSes, (a) $T_{w.z}$ and (b) $T_{w.y}$, vary with Π. The greyed areas, $-1<\log\Pi<1$, i.e. the sensitive zones, indicate where the data are strongly Π-dependent.